FIB-induced Gallium contamination as a tool to access aluminium crystallographic information from atom probe tomography data

William Mottay[a,b,*,1], Masoud Ahmadi[a], Nicolas Nothomb[a], Davide Vacirca[c], Matteo Ghidelli[c], Khalid Hoummada[b], Aude Simar[a,d] , Hosni Idrissi[a]

[a]IMMC, IMAP, Université Catholique de Louvain, 2 Place Sainte-Barbe, 1348 Louvain-La-Neuve, Belgium
[b]Aix-Marseille Université, CNRS, IM2NP, 142 Avenue Escadrille Normandie Niemen, 13013 Marseille, France
[c]LSPM, Université Sorbonne Paris Nord, 99 avenue J.B. Clement, Villetaneuse 93430, France
[d]WEL Research Institute, Wavre 1300, Belgium

*Corresponding author: william.mottay@uclouvain.be ; william.mottay@emse.fr

Abstract

Atom probe tomography (APT) provides three-dimensional compositional mapping of materials at near-atomic resolution, yet the information content of APT datasets is strongly influenced by specimen preparation. Notably, Gallium (Ga) implantation during focused ion beam (FIB) milling is generally considered a limitation that complicates data analyses, particularly in aluminium. In this work, we show that Ga implantation can instead be exploited as a sensitive marker to access additional microstructural and crystallographic information directly from APT data. Using aluminium-based systems as model materials, we demonstrate that Ga segregation is highly dependent on interface structure and crystalline defect character. In additively manufactured Al-7075, Ga selectively segregates at incoherent η precipitate interfaces while remaining absent at coherent η′ interfaces, enabling precipitates coherency and nature to be inferred solely from APT measurements. In sputtered multilayer thin films composed of alternating Al and high-entropy alloy (HEA) layers, we use Ga segregation to highlight grain boundaries and reveal that Cu segregation does not occur on all grain boundaries in the Al layers. Indeed, low-angle grain boundaries, as characterized by Ga segregation on dislocations lines, remain Cu-free and would not have been evidenced without Ga contamination. These results demonstrate that Ga implantation, traditionally regarded as a limitation of FIB-prepared APT specimens, can be repurposed as an intrinsic contrast agent. More broadly, this approach extends the information accessible from APT by providing indirect sensitivity to crystallographic information without relying on complementary crystallographic techniques.

Keywords

Atom probe tomography, Focus ion beam, Aluminium, Interfaces, Segregation, Transmission electron microscopy

Highlights

- Ga contamination reveals crystallographic data from APT analyses on Al alloys
- Coherent interfaces are free from Ga segregation, contrary to incoherent ones
- Grain boundaries free from solute segregation are revealed by Ga contamination

1 – Present address: Mines Saint-Etienne, Univ Lyon, CNRS, UMR 5307 LGF, Centre SMS, 158 cours Fauriel, Saint-Etienne, 42023, France, william.mottay@emse.fr

- Ga segregation is used to distinguish between low and high angle grain boundaries

1. Introduction

Atom probe tomography (APT) has become an essential characterization technique for materials science, offering three-dimensional (3D) compositional mapping with near-atomic spatial resolution and excellent chemical sensitivity [1–4]. APT enables direct visualization of solute distributions, nanoscale clustering, and segregation at interfaces, making it particularly suited to the study of complex microstructures such as those found in metallic alloys. Over the past decades, the technique has provided key insights into precipitation phenomena [5,6], solute partitioning [7], and atomic-scale interfacial chemistry [8,9] that were previously inaccessible by conventional microscopy.

Despite these advantages, one of the principal limitations of APT lies in its restricted access to crystallographic information. In contrast to transmission electron microscopy (TEM) or electron backscatter diffraction, which can directly reveal crystal orientation, defects, and interface coherency, APT primarily yields chemical data. Local solute enrichments can be used to detect crystalline defects, such as dislocations [10,11], grain boundaries [8,12] or precipitates [5,6], but these crystallographic data remain scarce and imprecise. For instance, it might be difficult to distinguish an elongated precipitate from a dislocation [5,13] and dislocations are indirectly detected by the segregated solutes around them [14]. While the presence of crystallographic poles and atomic planes in the reconstructed dataset can occasionally be used to infer orientation [10,15,16], such features depend strongly on the specimen geometry and field-evaporation behaviour and are not always present or well-defined. Consequently, direct correlation between chemical and crystallographic information remains challenging, limiting the ability of APT to fully describe structure–property relationships.

Aluminium (Al) alloys represent one of the most important classes of structural materials owing to their outstanding strength-to-weight ratio, corrosion resistance, and ease of processing [17–19]. Their mechanical performance is commonly enhanced through precipitation hardening, in which nanoscale solute-rich precipitates form during controlled heat treatments. The size, composition, and coherency of these precipitates play a decisive role in determining the mechanical properties of the alloy [6,20]. Understanding the precipitation sequence, from solute clusters to Guinier-Preston zones, η′, and η phases in 7xxx alloys [21–23], as well as whether precipitates form homogeneously or heterogeneously [24], is critical for alloy design and performance optimization. Besides, Al thin films are also used in nanolaminated materials to improve the trade-off between strength, ductility and fracture toughness [25–27].

Even though APT has been widely employed to investigate precipitation phenomena in Al alloys [6,21], several aspects of the precipitation sequence, such as the transformation pathways between η′ and η phases in Al–Zn–Mg–Cu alloys, remain under discussion [28]. Moreover, APT analyses of Al alloys face several experimental challenges. In Al-Zr alloys, the substantially higher evaporation field of Zr and Al_3Zr relative to the Al matrix [29,30] alters local evaporation conditions, leading to peak broadening and complex ion formation that complicate mass spectrum interpretation and quantification. A further and often critical issue arises from specimen preparation: APT tips are typically obtained by focused ion beam (FIB) milling using gallium (Ga) ions, which readily implant into the specimen surface [31,32].

Gallium contamination is particularly problematic in aluminium-based materials. Owing to its high diffusivity and strong tendency to segregate at defects and interfaces, Ga can redistribute within the Al matrix during specimen preparation or analysis [33]. This contamination can obscure genuine solute distributions, alter interfacial chemistry, and complicate the interpretation of APT data [34]. Consequently, most studies aim to minimize Ga incorporation by using low-energy cleaning steps [35], plasma FIB preparation, or alternative ion sources [34,36]

In the present work, we adopt a fundamentally different approach. Instead of mitigating Ga contamination, we intentionally exploit it as a structural probe. We demonstrate that Ga segregation behaviour within APT datasets can provide indirect yet highly informative crystallographic and interfacial data. It was previously shown by Aboulfadl et al. [37] that Ga could be used to detect dislocations in a recrystallized Al-Mg alloy, but no more crystallographic details were given. In this work, we demonstrate that in additively manufactured 7075 Al alloys, Ga segregates preferentially at incoherent η precipitate interfaces but not around coherent η′ precipitates, enabling direct inference of precipitate coherency from APT data alone. The nature of the precipitates as well as interface coherency is confirmed by TEM characterization. In sputtered Al–high-entropy alloy (Al-HEA) nanolaminates, Ga enrichment delineates specific grain boundaries, distinguishing those that host Cu segregation from those that do not, and revealing low-angle boundaries that are otherwise undetectable.

This work introduces a novel concept: the use of Ga contamination as a crystallographic marker in APT analyses of aluminium alloys**.** To the best of our knowledge, this is the first demonstration that detailed crystallographic information, traditionally inaccessible by APT, can be obtained directly from the APT dataset itself, without complementary microscopy. By transforming what is typically regarded as a limitation of FIB-based specimen preparation into a source of valuable structural information, this study opens new possibilities for correlating chemical and crystallographic data at the nanoscale in aluminium and other materials.

2. Materials and methods

2.1. Materials

A pre-alloyed modified Al7075 with Zn, Mg and Zr (AlCr0.3Cu1.5Mg4.1Zn6.7Zr0.9, from NANOVAL GmbH & Co. KG, Germany) was used for the L-PBF processing. The 7075 Al-alloy samples were processed using a ProX®DMP 200 system (3D Systems Inc., USA) with the following laser specifications: 1075 nm wavelength, 70 µm spot size, and 273 W maximum power. A non-heated 141 mm x 141 mm Al5Mg (wt% Mg) build plate was used. The O_2 content was maintained below 500 ppm by purging with Ar gas. The fully dense specimen (>99.5% relative density) underwent a classical T6 heat treatment composed of a first step for 1 h at 470°C in a Nabertherm furnace followed by water quenching and of a second step for 24 h at 120°C in a Binder oven.

The Al/HEA nanolaminates were deposited by magnetron sputtering on a Si (1 0 0) substrate using a 2" Al target (purity >99.95%) and a 2" CoCrCuFeNi target (purity >99.95%). The deposition was performed at room temperature, maintaining a target-substrate distance of 9 cm and a deposition pressure of 0.5 Pa. The CoCrCuFeNi and the Al layers were deposited by applying a power of 200 and 100 W, respectively. The individual layer thickness was set to 50 nm for each layer, with a total film thickness of 800 nm.

2.2. TEM sample preparation and analysis

TEM experiments were performed using a Talos microscope (Thermo Scientific) operated at an accelerating voltage of 200 kV. TEM imaging was carried out with a beam current of 3 nA, utilizing a 150 µm condenser aperture and a spot size of 3. Scanning transmission electron microscopy coupled with energy-dispersive X-ray spectroscopy (STEM-EDX) mapping was conducted in scanning mode using a beam current of 200 pA, a 70 µm condenser aperture, and a spot size of 7.

Foil specimens for TEM and STEM analyses were prepared using a Gatan Precision Ion Polishing System (PIPS). The samples were initially mechanically polished to a thickness of approximately 60 µm, followed by ion milling in the PIPS system with voltages gradually reduced from 5 kV to 1 kV, using a cascading milling angle from 5° to 1°.

2.3. APT sample preparation and APT analysis

Samples for APT analyses were prepared using a dual beam SEM/FIB FEI Helios Nanolab 600, following the standard lift-out procedure, including three annular milling steps at 30 kV and one cleaning step at 5 kV [38]. APT analyses were performed on a CAMECA LEAP 6000 XR in laser mode (i) with a 30 pJ laser energy, 25 K base temperature, 200 kHz pulse rate and 0.5 % detection rate for the Al-alloy and (ii) with a 30 pJ laser energy, 50 K base temperature, 200 kHz pulse rate and 2% detection rate for the Al/HEA thin films. Data were reconstructed using the APSuite software.

2.4. APT peak identification

For the Al-alloy, the main identified peaks in the mass spectra correspond to Al (9 Da, 13.5 Da and 27 Da), Mg (12 Da, 12.5 Da, 13 Da for Mg^{2+} and 24 Da, 25 Da, 26 Da for Mg^{+}), Zn (64, 66, 67, 68, 70 Da for Zn^{+} and 32, 33, 33.5, 34, 35 Da for Zn^{2+}), Cu (63, 65 Da for Cu^{+} and 31.5, 32.5 Da for Cu^{2+}) and Ga (34.5 Da and 69 Da). There is thus no overlap between the main alloying elements, nor with Ga, which originates from FIB-contamination.

Regarding the Al-HEA nanolaminates, only the Al layers are considered in this work. Therefore, the mass spectra present peaks corresponding only to Al (9 Da, 13.5 Da and 27 Da). Traces of other elements are also detected, Cu (63, 65 Da for Cu^{+} and 31.5, 32.5 Da for Cu^{2+}) and Ga (34.5 Da and 69 Da).

3. Results

3.1. 7075 Al-alloy

Figure 1 presents a typical 3D reconstructed APT tip from an additively manufactured 7075 Al-alloy. The 3D atom maps of Al (blue), Cu (orange), Mg (purple) and Zn (grey) are shown. Cu enrichment is found along a plane crossing the APT specimen, revealing a grain boundary in the APT sample. Multiple Mg and Zn enrichments highlight the presence of MgZn precipitates, both in the matrix and on the grain boundary (GB). The GB precipitates are larger and slightly enriched in Cu. In agreement with results available in the literature, these MgZn precipitates are most probably η or η' [39,40].

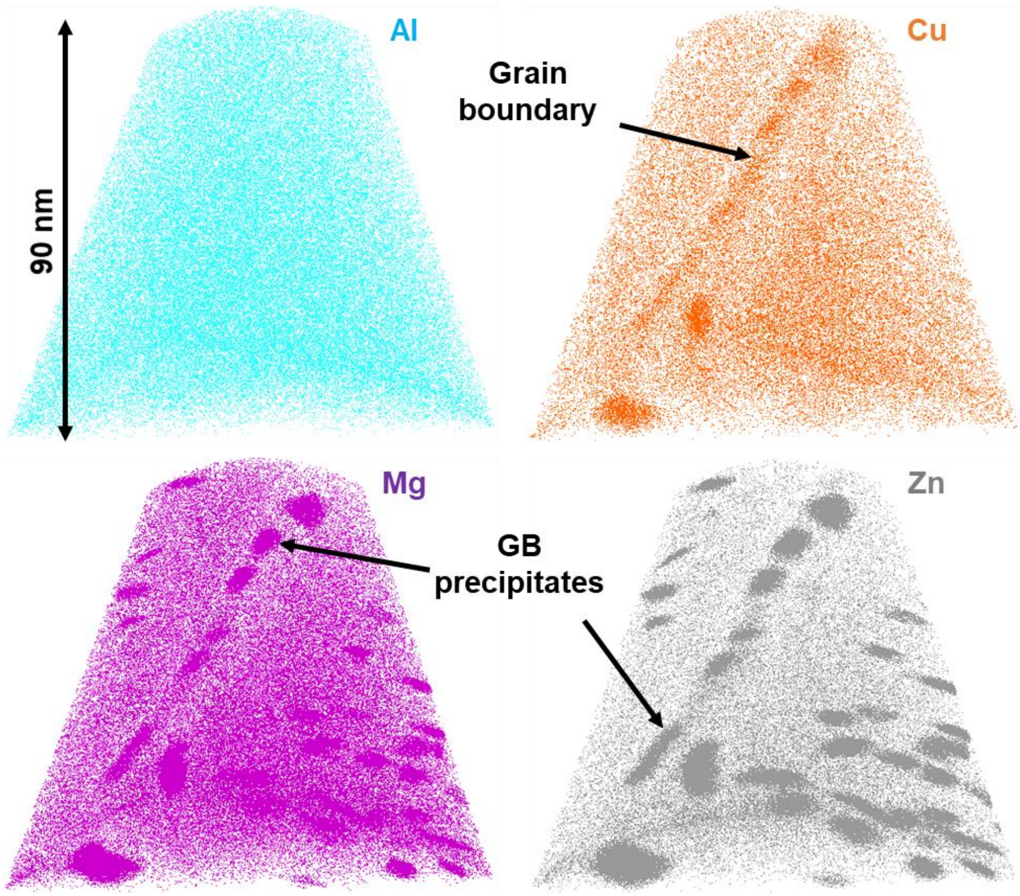

Figure 1 : Atom maps obtained by atom probe tomography on the 7075 Al-alloy. *Al atoms are displayed in blue, Cu in orange, Mg in purple and Zn in grey. Cu segregates and precipitates on the grain boundary. Mg and Zn precipitate both in the solid solution and on the grain boundary.*

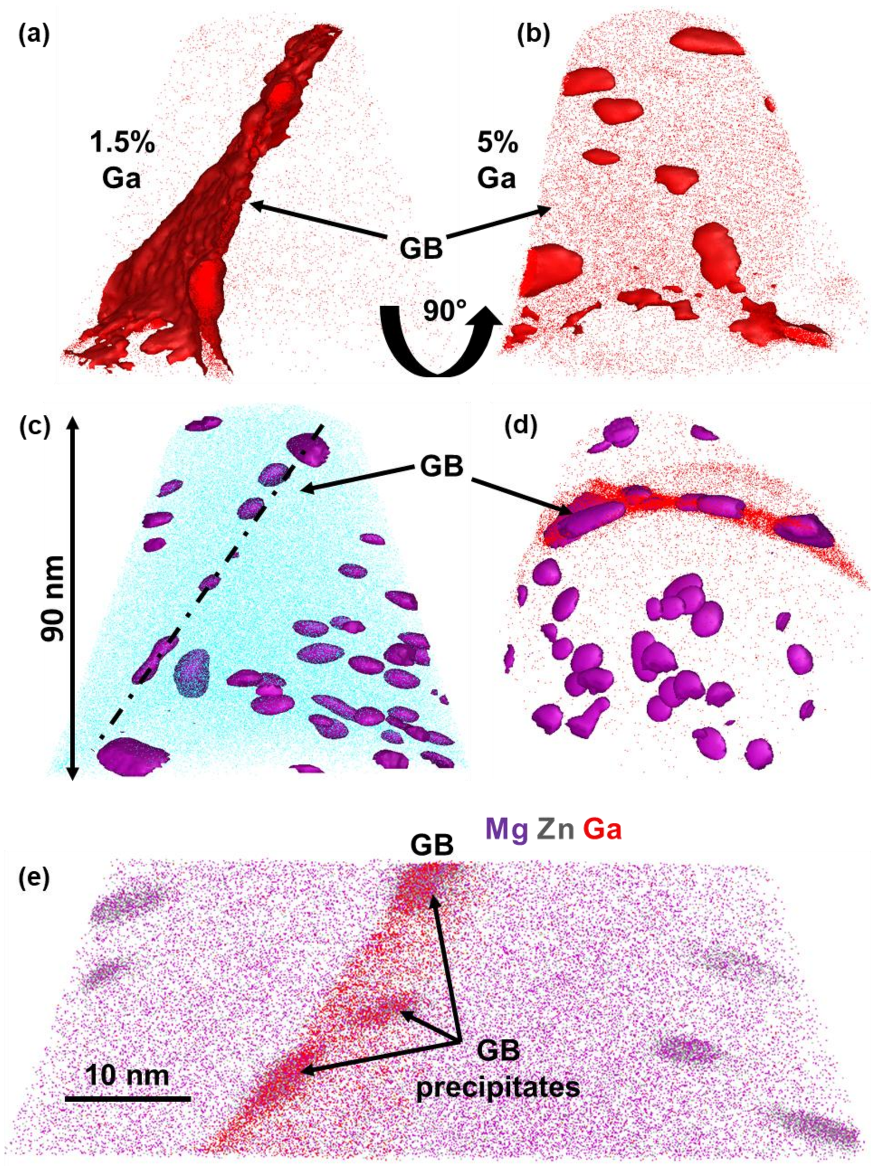

Figure 2 : Calculated iso-surfaces revealing MgZn precipitates and Ga segregation. *(a) 1.5 at.% Ga iso-concentration revealing Ga segregation on the grain boundary crossing the APT tip. (b) 5 at.% Ga iso-concentration showing Ga 'precipitates' on the grain boundary. (c) 20 at.% (Mg+Zn) iso-concentrations, evidencing the MgZn precipitates, superimposed to Al atom map. (d) Superposition of (Mg + Zn) iso-concentrations and Ga atom map. (e) Slice view of Mg, Zn and Ga atom maps uncovering that matrix MgZn precipitates are Ga-free while GB precipitates are Ga-rich.*

As stated in "Materials and Methods", section 2.3., the APT specimens were prepared by Ga-FIB. As could be expected, Ga contamination occurs during tip preparation by FIB and is thus detected during APT analysis, as shown in Figure 2, which represents a single APT tip, the same as in Figure 1. Ga atoms are detected in the 3D reconstructed APT volume, mostly on the grain boundary (Fig. 2a), where the grain boundary is highlighted by a 1.5 % Ga iso-concentration displayed in red. In-depth analyses of Ga distribution reveals that Ga "clusters" are found on the GB, as shown by the 5 at.% Ga iso-concentration from Figure 2b. Figure 2c represents the η / η' precipitates, readily observed on the atom maps from Figure 1, using a 20% iso-concentration of (Mg+Zn). Interestingly, most of the precipitates are free from Ga segregation at their interfaces with the matrix. This is illustrated in Figure 2d, which is a top view of the APT tip, where 20% iso-concentrations of (Mg+Zn) are superimposed to Ga atom maps. Except for the GB precipitates, MgZn particles do not seem contaminated by Ga atoms. This is confirmed by Figure 2e, which presents a slice of the APT volume, where Mg, Zn and Ga atoms are observed. This uncovers that homogeneous MgZn precipitates, in the matrix, are not contaminated by Ga, while the precipitates on the GB are enriched in Ga. Two hypotheses can be formulated: (i) Ga enrichment around precipitates is kinetically limited. Then, Ga is not found in matrix precipitates, only on GB ones, since the GB accelerates Ga diffusion. (ii) There are structural differences between the matrix and GB precipitates which make them unfavorable, respectively favorable, for Ga enrichment. These hypotheses will be further investigated in this section and discussed in section 4.1.

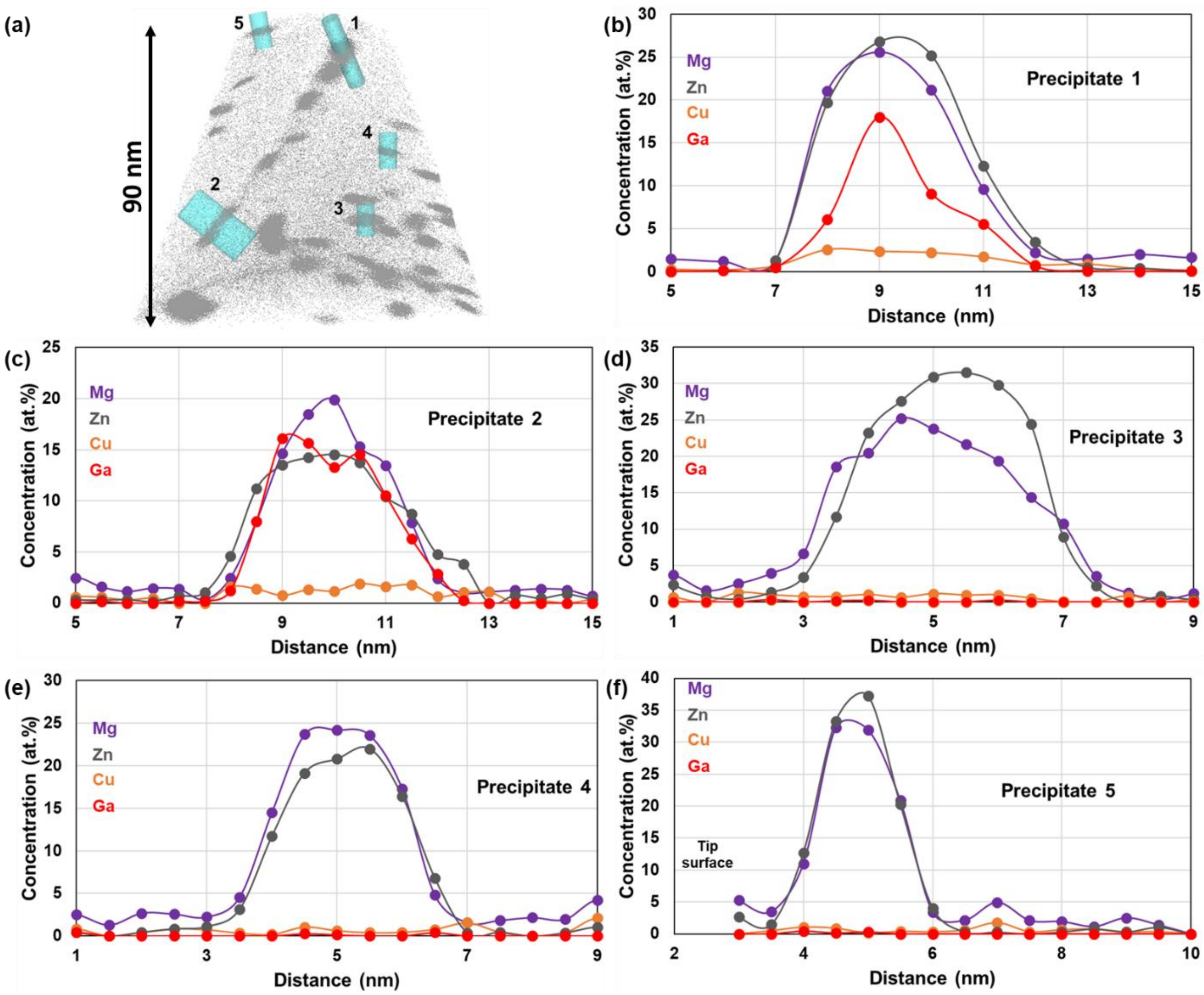

Figure 3 : 1D concentration profiles across 5 different precipitates. *(a) Identification of the 5 precipitates from Zn atom map. Precipitates 1 and 2 are GB precipitates while precipitates 3 and 4 are found in the matrix. Precipitate 5 is also a homogeneous precipitate, but close to the tip surface. (b-f) Concentration profiles across the 5 precipitates. Precipitates 1 and 2 (b-c) exhibit Ga contamination. Precipitates 3 and 4 (d-e) are free from Ga contamination, as well as precipitate 5 (f) even though it is close to the tip surface.*

Ga contamination around the different precipitates is further investigated in Figure 3. 1D concentration profiles across 5 different precipitates were plotted. Precipitates 1 and 2 are GB precipitates, while 3 and 4 are intragranular precipitates. Precipitate 5 is also a matrix precipitate, but close to the tip surface (about 1 nm). The 1D concentration profiles across the GB precipitates (1 and 2, Fig. 3b and 3c) reveal that Ga is detected in these precipitates. It is not clear from APT data whether Ga is found in the precipitates or at the interfaces. These discrepancies arise from well-known APT artifacts: differences in field evaporation between the precipitates and the matrix, between Ga ions and other ions, trajectory aberrations at the GB [1,15]. It is also worth noting that these precipitates are slightly enriched in Cu (about 2% at). Interestingly, 1D concentration profiles across the homogeneous precipitates 3 and 4 (Fig. 3d and 3e) provide different results. The Mg to Zn ratio is the same, close to 1, whatever the considered precipitates. However, intragranular precipitates are free from Cu and Ga. The absence of Ga contamination could rely on kinetic considerations, i.e. the investigated precipitates are too far away in the volume. To determine that, a 1D concentration profile was also calculated for precipitate 5 (Fig. 3f), which is close the tip surface and close to the apex, about 1 nm away. Interestingly, and surprisingly, Ga is not found either in this homogeneous precipitate. It can then be concluded that the absence of Ga in the matrix precipitates does not rely on kinetic limitations. It is worth noting that this precipitate is also Cu-free.

Complementary TEM analyses were performed on the additively manufactured 7075 Al-alloy. Figure 4a presents HAADF and STEM-EDX maps, which reveal MgZn-rich precipitates, corresponding to η / η’, in accordance with the APT results. These precipitates are found both on grain boundaries and inside the Al matrix, but the GB precipitates are also enriched in Cu, in agreement with the results from Figure 3. Figure 4b presents a HR-TEM micrograph which shows the presence of a precipitate on Al grain boundary. FFTs demonstrate that this precipitate is η type, which is incoherent with respect to the Al matrix. Conversely, Figure 4c presents a HR-TEM micrograph of a matrix precipitate, which appears to be a η’ precipitate, coherent with the Al matrix, as proven by FFTs. Consequently, TEM analyses demonstrate that MgZn-rich precipitates on grain boundaries are incoherent η enriched in Cu, while MgZn-rich precipitates in the matrix are incoherent η’, nearly free from Cu enrichment.

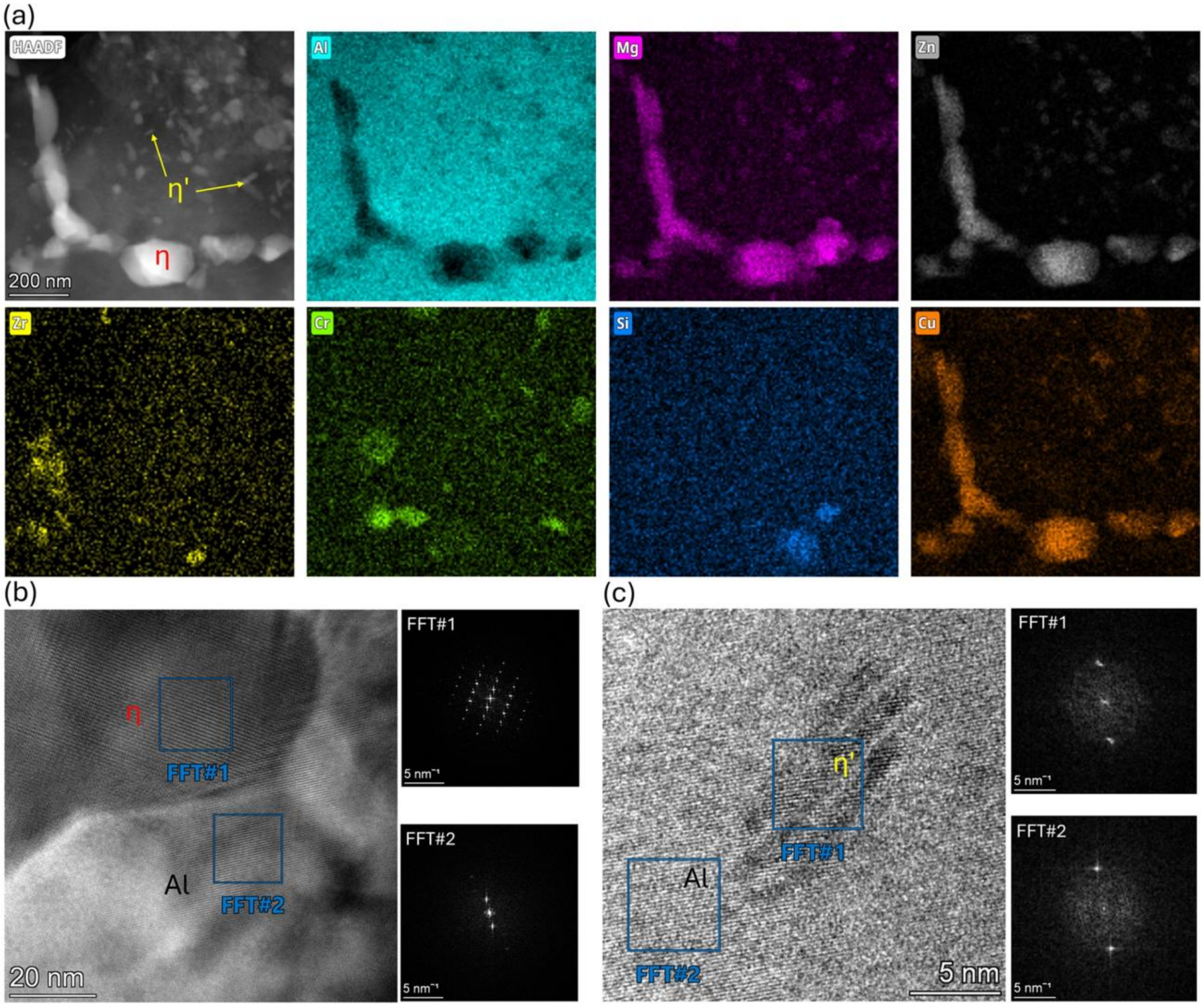

Figure 4 : TEM micrographs collected in the additively manufactured 7075 Al-alloy. *(a) HAADF and STEM-EDX maps showing η precipitates on grain boundaries and η' inside the Al matrix. η precipitates on grain boundaries are enriched in Cu. (b) HR-TEM micrograph and FFTs demonstrating the incoherency of η precipitates on GBs. (c) HR-TEM micrograph and FFTs evidencing the coherency of η' precipitates found in the Al matrix.*

In conclusion, the results from the correlative APT-TEM analyses reveal that two types of MgZn precipitates are found in the 7075 Al-alloy, (i) incoherent η precipitates, found on GB and Cu-enriched and (ii) coherent η', precipitated in the matrix and free from Cu. Interestingly, these two precipitates could have been readily distinguished from APT data, based on Ga segregation at their interfaces. This point is further detailed in the "Discussion" part, section 4.1.

3.2. Al-HEA nanolaminates

Figure 5 presents a typical APT reconstructed volume of the Al/HEA nanolaminates. The Al layers being nearly pure aluminum, they are sensitive to Ga contamination during FIB preparation. Further investigations of Ga implantation in these Al layers are presented in Figures 6 and 7.

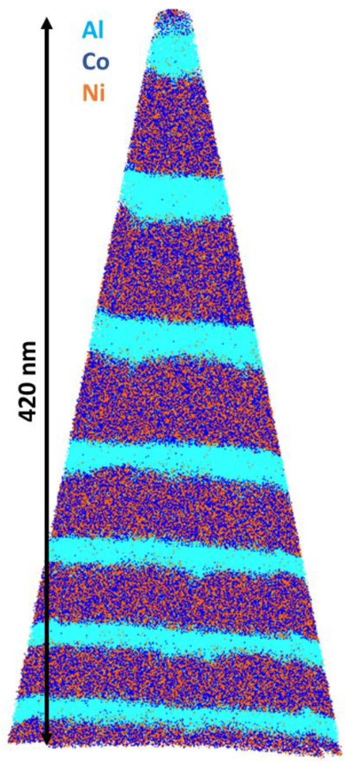

Figure 5 : Typical APT data collected on the Al-HEA nanolaminates. *Only Al, Co and Ni are represented, since there are overlaps between Cr, Fe and Al peaks. Al atoms, found in the Al layer are displayed in cyan. Co and Ni are represented in dark blue and orange respectively. They are found in the HEA layers, which will not be further investigated here as it is out of the scope of this work.*

The top view of an Al layer is shown in Figure 6. In this layer, Al atoms are displayed in cyan, Cu in black and Ga in red. The Cu enrichment is explained by the diffusion of Cu from the surrounding HEA layers during the sputtering process, favored by the negative mixing enthalpy of Cu in Al [41]. As expected from Cu and Ga, they tend to segregate on Al grain boundaries. However, a detailed comparison of Cu and Ga atom maps reveal that some Al boundaries, marked by the red arrows in Figure 6, are enriched in Ga but free from Cu. Thus, Ga contamination could be used to reveal grain boundaries in Al-based alloys from APT data, even if the grain boundaries are free from solute segregation. In the present case, Ga segregation in the Al layers can be used to determine the Al grain size with better accuracy than with Cu.

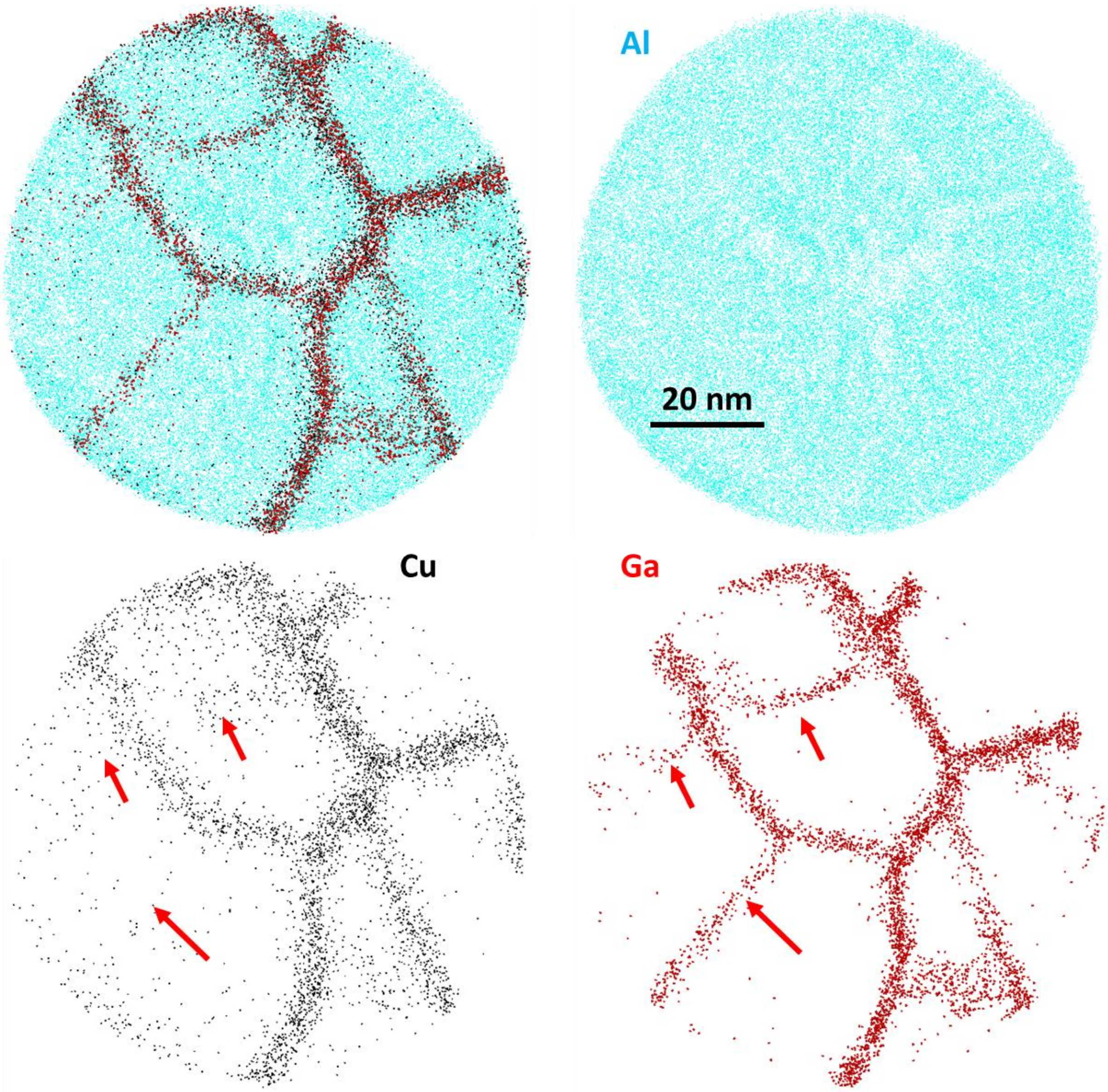

Figure 6 : Top view of an Al layer, revealing Cu and Ga segregation at Al grain boundaries. *In-depth investigations reveal that Cu is found only in some of the grain boundaries, as marked by the red arrows. The remaining Cu-free grain boundaries are revealed by Ga contamination.*

Another Al layer is presented in Figure 7, in which a Cu and Ga segregated grain boundary can be observed. Detailed analysis of the grain boundary reveals that the segregation occurs along parallel lines in the grain boundary plane. This can be interpreted as a low angle grain boundary, which is characterized by a network of parallel dislocations [42–44]. Interestingly, when looking at the atom maps of Cu and Ga, it appears that Cu enrichment on the grain boundary does not allow visualizing the dislocation network, contrary to Ga segregation, in accordance with [37]. Once again, Ga provides more detailed crystallographic information readily from APT data, which can be used to refine the modeling of materials mechanical properties at small scales.

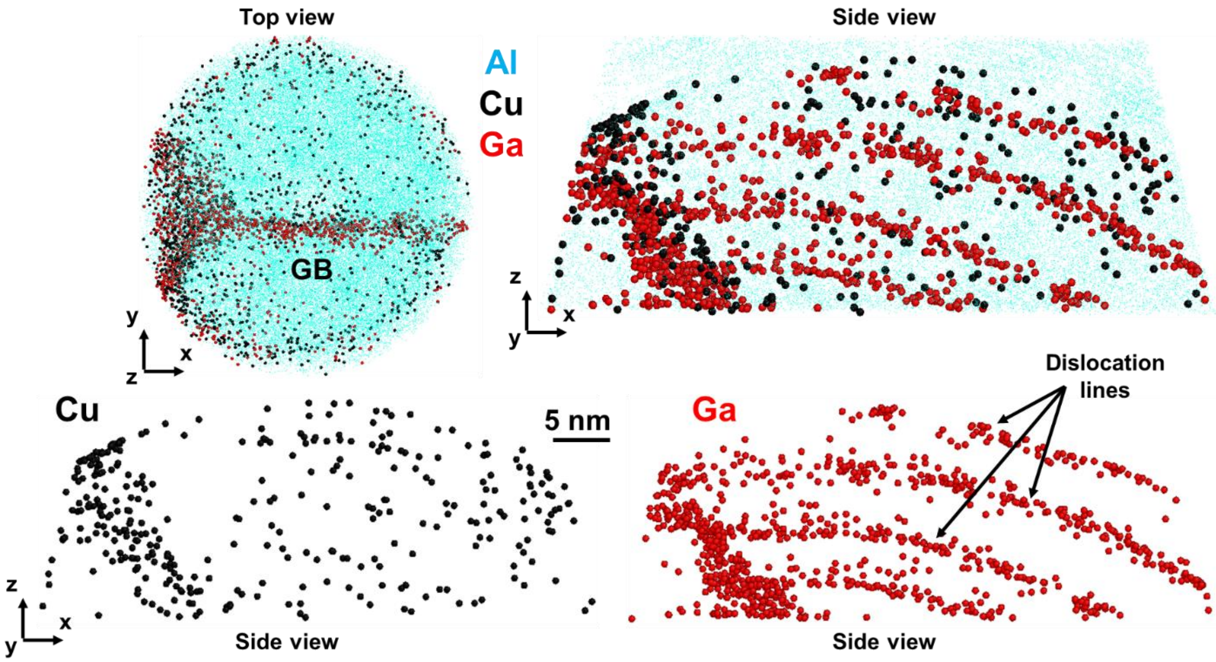

Figure 7 : Cu and Ga segregation at a low-angle grain boundary. *Top view of the Al layer evidences Cu and Ga segregation on a grain boundary. Orthogonal visualization of the GB evidences a dislocation network in the GB plane, demonstrating that the GB is a low-angle one. The dislocation network is evidenced solely by Ga atoms, not by Cu.*

4. Discussion

The results from the present work reveal interesting insights regarding Ga contamination, due to FIB preparation, around precipitates in a 7075 Al-alloy. As evidenced in Figure 1, numerous Mg and Zn rich precipitates are found in the APT tips. They are distributed homogeneously in the Al matrix but also located on crystalline defects, such as grain boundaries (Fig. 1 and 2). The latter precipitates are slightly enriched in Cu (Figures 3 and 4). In accordance with results available in the literature, and confirmed by TEM observations presented in Figure 4, these are η / η' precipitates [23,40]. It was demonstrated that η precipitates are stable, whereas η' are metastable. These two precipitates can be distinguished by two aspects. From a crystallographic point of view, the metastable η' are coherent with respect to the Al matrix, while the stable η precipitates lose their coherency with the Al matrix during heat treatments. Besides, from a chemical aspect, η' are nearly exclusively composed of Mg and Zn atoms, while η precipitates can be enriched in solute atoms, notably Cu [45]. Thus, the MgZn rich precipitates observed in the Al matrix are η' precipitates, since they are coherent with the Al matrix (Figure 4) and not enriched in solute atoms (Figure 3 and 4). However, the MgZn rich precipitates on the grain boundary are stable η precipitates, since they are incoherent with the Al matrix and slightly enriched in Cu. The presence of stable η precipitates on the GB is not surprising, as GBs and overall crystal defects act as diffusion short-circuits [46] and thus accelerate the transformation from η' to η.

Interestingly, the distinction between η' and η precipitates could be directly deduced from APT data. On the one hand, concentration profiles of the GB precipitates reveal a copper enrichment inside the precipitates, which is characteristic of stable η precipitates, even though it could be argued that the detected Cu inside the precipitates rather comes from segregated Cu on the grain boundary. On the other hand, Ga is detected only on the GB precipitates. The presence of Ga inside the precipitates, as seen in the concentration profiles (Fig. 4b and 4c), is highly unexpected, since Ga is a contamination coming from FIB preparation. Ga is most probably located at the interface between the precipitates and the matrix, but wrongly reconstructed inside the precipitates because of local variations in applied electric field and trajectory aberrations, due to the presence a grain boundary and a precipitate [1,15]. Yet, it appears rather surprising that Ga segregates only around the GB precipitates. This could rely on kinetic considerations: Ga does not diffuse fast enough to segregate around the matrix precipitate, contrary to the GB which acts as a diffusion short-circuit and thus allows for Ga segregation around GB precipitates. This argument is invalid since Ga is known to diffuse fast in Al alloys [47–49]. Moreover, Ga is not found around the matrix precipitates close to the tip surface, Fig. 3f.

As a consequence, we conclude that Ga segregates only around GB precipitates for thermodynamic reasons, i.e. the interfaces of these precipitates are favorable to Ga segregation, contrary to the interfaces of the matrix precipitates. This conclusion is strengthened by TEM observations (Fig. 4) which show that the precipitate / matrix interfaces are different (coherent or incoherent) between the two types of precipitates. The results from the present work, in accordance with the ones available in the literature [50,51], provide evidence that GB precipitates exhibit an incoherent interface while the matrix precipitates have a coherent interface. This can be fully explained by generated lattice misfits, rather important in the case of incoherent precipitates, negligible when dealing with coherent interfaces [52]. Consequently, Ga cannot segregate at coherent interfaces, but will enrich incoherent interfaces.

Based on these elements, it would be possible, solely from APT data, to draw major conclusions regarding the η / η' precipitates in the APT tip. Since Ga is found segregated around GB precipitates, we can state that these precipitates are incoherent with the Al matrix, contrary to the matrix precipitates which are coherent. These crystallographic differences are deduced indirectly from chemical data, the segregation of Ga on the aforementioned interfaces. First, the identification of interfaces nature allows distinguishing η from η' readily from the chemical data collected using APT. Second, considering that the interaction between dislocations and crystal defects (precipitates, grain boundaries …) depends on the nature of the interface [53], it is possible to enrich models of mechanical properties at the nano-scale based exclusively on the APT data. Therefore, we propose that Ga can be used as a tool to determine precipitates / matrix coherency readily from APT data, without complementary data analyses.

Complementary results from the present work on a fully different material, namely the Al-HEA nanolaminates, demonstrate that is is possible to exploit Ga contamination during FIB preparation to indirectly access some other precise crystallographic data, such as grain boundary nature, or grain size. Indeed, on grain boundaries segregated by both Cu and Ga, we show in Figure 7 that Ga is the only element able to reveal the network of parallel dislocations, thus evidencing the exact nature of the interface, a low-angle grain boundary. Besides, it appears possible to determine a grain size, especially for multilayer or nano-crystalline materials thanks to Ga contamination. Even if GBs are not segregated by solute atoms (here Cu), Ga contamination allows revealing GBs, and thus estimating a grain size, at least in Al-based materials. Once again, these elements are deduced readily from APT data, without any supplementary experimental techniques. These results are therefore valuable for advancing material characterization and strengthening the input data for mechanical modeling [54].

5. Conclusion

In this work, different Al-based materials are investigated using APT after contamination by Ga^+ during FIB preparation. We demonstrate that this approach can be used as a tool to reveal precise microstructural information of the investigated material, readily from APT data. For instance, in a 7075 Al-alloy, η and η' precipitates, which only differ by their coherency with respect to the Al matrix, can be distinguished directly from APT data, based on Ga segregation. Indeed, Ga segregates only on the incoherent interfaces, corresponding to η, but coherent interfaces, corresponding to η', are free from Ga. Moreover, in Al-HEA nanolaminates, more grain boundaries are revealed by Ga enrichment than by Cu segregation. Ga segregation at grain boundaries also highlights low-angle boundaries that are otherwise undetectable by APT. Overall, detailed crystallographic information can be obtained directly from the APT dataset, without complementary microscopy, allowing for improved microstructural characterization using a single experimental technique.

Acknowledgements

W.M., MA, N.N., A.S and H.I. acknowledge the financial support from the Wallinov GreenAl project (convention n°2310011) funded by the Service Public de Wallonie, Economie Emploi Recherche (SPW-EER), Belgium. H.I. is mandated by the Belgian National Fund for Scientific Research (FSR-FNRS). This project was also supported by the European Union through the program PIIEC ME/CT (project SCIRIUS, No. DOS0217953). D.V. and M.G. acknowledge the ANR-JCJC project Micro-HEAs (grant agreement no. ANR-21-CE08-0003-01).

Data availability

Research data is available upon request to the corresponding author.

References

[1] B. Gault, M.P. Moody, J.M. Cairney, S.P. Ringer, Atom Probe Microscopy, Springer New York, New York, NY, 2012. https://doi.org/10.1007/978-1-4614-3436-8.

[2] B. Gault, A. Chiaramonti, O. Cojocaru-Mirédin, P. Stender, R. Dubosq, C. Freysoldt, S.K. Makineni, T. Li, M. Moody, J.M. Cairney, Atom probe tomography, Nat. Rev. Methods Primer 1 (2021) 51. https://doi.org/10.1038/s43586-021-00047-w.

[3] B. Gault, M.P. Moody, F. De Geuser, A. La Fontaine, L.T. Stephenson, D. Haley, S.P. Ringer, Spatial Resolution in Atom Probe Tomography, Microsc. Microanal. 16 (2010) 99–110. https://doi.org/10.1017/S1431927609991267.

[4] T.F. Kelly, M.K. Miller, Atom probe tomography, Rev. Sci. Instrum. 78 (2007) 031101. https://doi.org/10.1063/1.2709758.

[5] J. Landes, W. Mottay, K. Hoummada, C. Perrin, V. Massardier, M. Jouiad, N. Hervé, A. Marceaux Dit Clément, P. Maugis, Precipitation of Manganese Nitride During Post-Weld Heat Treatment in C-Mn and Low-Alloy Steel Welds, Metall. Mater. Trans. A (2025). https://doi.org/10.1007/s11661-025-07694-8.

[6] Z. Zhu, F.L. Ng, H.L. Seet, W. Lu, C.H. Liebscher, Z. Rao, D. Raabe, S. Mui Ling Nai, Superior mechanical properties of a selective-laser-melted AlZnMgCuScZr alloy enabled by a tunable hierarchical microstructure and dual-nanoprecipitation, Mater. Today 52 (2022) 90–101. https://doi.org/10.1016/j.mattod.2021.11.019.

[7] P.A.J. Bagot, O.B.W. Silk, J.O. Douglas, S. Pedrazzini, D.J. Crudden, T.L. Martin, M.C. Hardy, M.P. Moody, R.C. Reed, An Atom Probe Tomography study of site preference and partitioning in a nickel-based superalloy, Acta Mater. 125 (2017) 156–165. https://doi.org/10.1016/j.actamat.2016.11.053.

[8] W. Mottay, D. Caillard, H. Idrissi, P. Maugis, A. Portavoce, F. Roch, C. Perrin-Pellegrino, K. Hoummada, Investigation of the influence of manganese on the dynamic strain ageing of ferritic steels – Part II: Industrial alloy, Acta Mater. 301 (2025) 121576. https://doi.org/10.1016/j.actamat.2025.121576.

[9] W. Mottay, P. Maugis, M. Jouiad, F. Roch, C. Perrin-Pellegrino, K. Hoummada, Effect of dislocation density on competitive segregation of solute atoms to dislocations, Mater. Sci. Eng. A 881 (2023) 145380. https://doi.org/10.1016/j.msea.2023.145380.

[10] D. Blavette, E. Cadel, A. Fraczkiewicz, A. Menand, Three-Dimensional Atomic-Scale Imaging of Impurity Segregation to Line Defects, Science 286 (1999) 2317–2319. https://doi.org/10.1126/science.286.5448.2317.

[11] M.K. Miller, Atom probe tomography characterization of solute segregation to dislocations, Microsc. Res. Tech. 69 (2006) 359–365. https://doi.org/10.1002/jemt.20291.

[12] E.A. Marquis, N.A. Yahya, D.J. Larson, M.K. Miller, R.I. Todd, Probing the improbable: imaging C atoms in alumina, Mater. Today 13 (2010) 34–36. https://doi.org/10.1016/S1369-7021(10)70184-X.

[13] E. Pereloma, V. Bata, A.A. Gazder, The effect of chromium addition on the strain ageing and recrystallisation behaviour of low carbon steel, (2012) 12.

[14] W. Mottay, J. Landes, A. Portavoce, B. Klaes, F. Danoix, P. Maugis, P. Stocker, C. Perrin-Pellegrino, K. Hoummada, Startling C Behavior in Mo-Free Steel Atom Probe Tomography Volumes, Microsc. Microanal. 31 (2025) ozaf078. https://doi.org/10.1093/mam/ozaf078.

[15] B. Gault, M.P. Moody, J.M. Cairney, S.P. Ringer, Atom probe crystallography, Mater. Today 15 (2012) 378–386. https://doi.org/10.1016/S1369-7021(12)70164-5.

[16] B. Gault, F. Danoix, K. Hoummada, D. Mangelinck, H. Leitner, Impact of directional walk on atom probe microanalysis, Ultramicroscopy 113 (2012) 182–191. https://doi.org/10.1016/j.ultramic.2011.06.005.

[17] P.A. Rometsch, Y. Zhu, X. Wu, A. Huang, Review of high-strength aluminium alloys for additive manufacturing by laser powder bed fusion, Mater. Des. 219 (2022) 110779. https://doi.org/10.1016/j.matdes.2022.110779.

[18] E. Georgantzia, M. Gkantou, G.S. Kamaris, Aluminium alloys as structural material: A review of research, Eng. Struct. 227 (2021) 111372. https://doi.org/10.1016/j.engstruct.2020.111372.

[19] C. Linder, B. Mehta, S. Sainis, J.B. Lindén, C. Zanella, L. Nyborg, Corrosion resistance of additively manufactured aluminium alloys for marine applications, Npj Mater. Degrad. 8 (2024) 46. https://doi.org/10.1038/s41529-024-00459-5.

[20] N. Nothomb, I. Rodriguez-Barber, M.-N. Avettand-Fénoël, M.T. Pérez Prado, M. Marinova, A. Simar, Understanding the effect of tailored heat treatment on Zr-modified Al7075 fabricated by laser powder bed fusion, Mater. Des. 258 (2025) 114553. https://doi.org/10.1016/j.matdes.2025.114553.

[21] H. Zhao, Y. Chen, B. Gault, S.K. Makineni, D. Ponge, D. Raabe, (Al, Zn)3Zr dispersoids assisted η′ precipitation in anAl-Zn-Mg-Cu-Zr alloy, Materialia 10 (2020) 100641. https://doi.org/10.1016/j.mtla.2020.100641.

[22] P. Priya, D.R. Johnson, M.J.M. Krane, Precipitation during cooling of 7XXX aluminum alloys, Comput. Mater. Sci. 139 (2017) 273–284. https://doi.org/10.1016/j.commatsci.2017.08.008.

[23] Z. Chen, K. Yan, C. Ren, S. Naseem, Precipitation sequence and hardening effect in 7A85 aluminum alloy, J. Alloys Compd. 875 (2021) 159950. https://doi.org/10.1016/j.jallcom.2021.159950.

[24] C. Gallais, A. Denquin, Y. Bréchet, G. Lapasset, Precipitation microstructures in an AA6056 aluminium alloy after friction stir welding: Characterisation and modelling, Mater. Sci. Eng. A 496 (2008) 77–89. https://doi.org/10.1016/j.msea.2008.06.033.

[25] T.E.J. Edwards, T. Xie, N. Maria Della Ventura, D. Casari, C. Guerra, E. Huszár, X. Maeder, J.J. Schwiedrzik, I. Utke, L. Pethö, J. Michler, On the thinnest Al2O3 interlayers in Al-based nanolaminates to enhance strength, and the role of constraint, Acta Mater. 240 (2022) 118345. https://doi.org/10.1016/j.actamat.2022.118345.

[26] P. Baral, S. Jaddi, H. Wang, A. Orekhov, N. Gauquelin, A. Bagherpour, F. Van Loock, M. Coulombier, A. Favache, M. Rusinowicz, J. Verbeeck, S. Lucas, J.-P. Raskin, H. Idrissi, T. Pardoen, Al2O3/Al hybrid nanolaminates with superior toughness, strength and ductility, Nat. Commun. 16 (2025) 1355. https://doi.org/10.1038/s41467-025-56512-7.

[27] C. Poltronieri, A. Brognara, C. Jung, F. Challali, P. Djemia, G. Dehm, J.P. Best, M. Ghidelli, Effect of chemical composition on mechanical properties and shear band propagation in fully-amorphous ZrCu/ZrCuAl nanolaminates, Scr. Mater. 259 (2025) 116571. https://doi.org/10.1016/j.scriptamat.2025.116571.

[28] S.J. Andersen, C.D. Marioara, J. Friis, S. Wenner, R. Holmestad, Precipitates in aluminium alloys, Adv. Phys. X 3 (2018) 1479984. https://doi.org/10.1080/23746149.2018.1479984.

[29] K.E. Knipling, D.C. Dunand, D.N. Seidman, Atom Probe Tomographic Studies of Precipitation in Al-0.1Zr-0.1Ti (at.%) Alloys, Microsc. Microanal. 13 (2007) 503–516. https://doi.org/10.1017/S1431927607070882.

[30] G. Sha, A. Cerezo, Field ion microscopy and 3-D atom probe analysis of Al3Zr particles in 7050 Al alloy, Ultramicroscopy 102 (2005) 151–159. https://doi.org/10.1016/j.ultramic.2004.09.006.

[31] A.W. Thompson, Z.D. Harris, J.T. Burns, Examination of focused ion beam-induced damage during platinum deposition in the near-surface region of an aerospace aluminum alloy, Micron 118 (2019) 43–49. https://doi.org/10.1016/j.micron.2018.12.004.

[32] E. Lang, K. Hattar, T. Richter, A. Nadzeyka, K. Hooghan, Deciphering Liquid Metal Embrittlement and Altered FIB Damage Microstructures on Aluminum, Microsc. Microanal. 27 (2021) 26–27. https://doi.org/10.1017/S1431927621000684.

[33] E. Senel, J.C. Walmsley, S. Diplas, K. Nisancioglu, Liquid metal embrittlement of aluminium by segregation of trace element gallium, Corros. Sci. 85 (2014) 167–173. https://doi.org/10.1016/j.corsci.2014.04.012.

[34] H.C. Jansen, A. Sharma, K. Wieczerzak, G.K. Nayak, J.M. Schneider, J. Schwiedrzik, T.E.J. Edwards, J. Michler, On the efficacy of Xe+-pFIB preparation to avoid Ga+-FIB induced phase transformations in Al-Ni alloys, Scr. Mater. 260 (2025) 116589. https://doi.org/10.1016/j.scriptamat.2025.116589.

[35] K. Thompson, B. Gorman, D. Larson, B.V. Leer, L. Hong, Minimization of Ga Induced FIB Damage Using Low Energy Clean-up, Microsc. Microanal. 12 (2006) 1736–1737. https://doi.org/10.1017/S1431927606065457.

[36] L. Lilensten, B. Gault, New approach for FIB-preparation of atom probe specimens for aluminum alloys, PLOS ONE 15 (2020) e0231179. https://doi.org/10.1371/journal.pone.0231179.

[37] H. Aboulfadl, J. Deges, P. Choi, D. Raabe, Dynamic strain aging studied at the atomic scale, Acta Mater. 86 (2015) 34–42. https://doi.org/10.1016/j.actamat.2014.12.028.

[38] D.J. Larson, T.J. Prosa, R.M. Ulfig, B.P. Geiser, T.F. Kelly, Local Electrode Atom Probe Tomography: A User's Guide, Springer New York, New York, NY, 2013. https://doi.org/10.1007/978-1-4614-8721-0.

[39] G. Sha, A. Cerezo, Early-stage precipitation in Al–Zn–Mg–Cu alloy (7050), Acta Mater. 52 (2004) 4503–4516. https://doi.org/10.1016/j.actamat.2004.06.025.

[40] X.Z. Li, V. Hansen, J. GjØnnes, L.R. Wallenberg, HREM study and structure modeling of the η′ phase, the hardening precipitates in commercial Al–Zn–Mg alloys, Acta Mater. 47 (1999) 2651–2659. https://doi.org/10.1016/S1359-6454(99)00138-X.

[41] N.A. Krapivka, S.A. Firstov, M.V. Karpets, A.N. Myslivchenko, V.F. Gorban', Features of phase and structure formation in high-entropy alloys of the AlCrFeCoNiCu x system (x = 0, 0.5, 1.0, 2.0, 3.0), Phys. Met. Metallogr. 116 (2015) 467–474. https://doi.org/10.1134/S0031918X15030084.

[42] V. Randle, H. Davies, I. Cross, Grain boundary misorientation distributions, Curr. Opin. Solid State Mater. Sci. 5 (2001) 3–8. https://doi.org/10.1016/S1359-0286(00)00018-8.

[43] A.P. Sutton, R.W. Balluffi, Interfaces in crystalline materials, Repr, Clarendon Press, Oxford, 2003.

[44] I. Medouni, A. Portavoce, P. Maugis, P. Eyméoud, M. Yescas, K. Hoummada, Role of dislocation elastic field on impurity segregation in Fe-based alloys, Sci. Rep. 11 (2021). https://doi.org/10.1038/s41598-020-80140-4.

[45] X. Zhang, Z. Han, L. Xu, H. Ni, X. Hu, H. Zhou, Y. Zou, J. Wang, Evolution of precipitate and precipitate/matrix interface in Al-Zn-Mg-Cu (-Ag) alloys, J. Mater. Sci. Technol. 138 (2023) 157–170. https://doi.org/10.1016/j.jmst.2022.07.049.

[46] H. Mehrer, ed., Diffusion in Solid Metals and Alloys, Springer-Verlag, Berlin/Heidelberg, 1990. https://doi.org/10.1007/b37801.

[47] R.C. Hugo, R.G. Hoagland, Gallium penetration of aluminum: in-situ TEM observations at the penetration front, Scr. Mater. 41 (1999) 1341–1346. https://doi.org/10.1016/S1359-6462(99)00293-6.

[48] K.A. Unocic, M.J. Mills, G.S. Daehn, Effect of gallium focused ion beam milling on preparation of aluminium thin foils, J. Microsc. 240 (2010) 227–238. https://doi.org/10.1111/j.1365-2818.2010.03401.x.

[49] J. Peng, T. Wang, Kinetics calculation of Al/Ga interfacial diffusion in sandwich geometry model, Vacuum 216 (2023) 112387. https://doi.org/10.1016/j.vacuum.2023.112387.

[50] R. Ferragut, A. Somoza, A. Tolley, Microstructural evolution of 7012 alloy during the early stages of artificial ageing, Acta Mater. 47 (1999) 4355–4364. https://doi.org/10.1016/S1359-6454(99)00315-8.
[51] T. Hu, K. Ma, T.D. Topping, J.M. Schoenung, E.J. Lavernia, Precipitation phenomena in an ultrafine-grained Al alloy, Acta Mater. 61 (2013) 2163–2178. https://doi.org/10.1016/j.actamat.2012.12.037.
[52] M.P. Seah, Grain boundary segregation, J. Phys. F Met. Phys. 10 (1980) 1043–1064. https://doi.org/10.1088/0305-4608/10/6/006.
[53] S.-H. Lee, T.-Y. Ahn, S.-I. Baik, D.N. Seidman, S.-J. Lee, Y.-K. Lee, K. Euh, J.-G. Jung, Unravelling precipitation behavior and mechanical properties of Al–Zn–Mg–Cu alloy, J. Mater. Sci. Technol. 204 (2025) 177–189. https://doi.org/10.1016/j.jmst.2024.03.021.
[54] N. Wang, Z. Wang, K.T. Aust, U. Erb, Effect of grain size on mechanical properties of nanocrystalline materials, Acta Metall. Mater. 43 (1995) 519–528. https://doi.org/10.1016/0956-7151(94)00253-E.